

## Secondary initiation of multiple bands of cumulonimbus over southern Britain. II: Dynamics of secondary initiation

By J. H. MARSHAM\* and D. J. PARKER  
*University of Leeds, UK*

(Received 18 July 2005; revised 5 December 2005)

### SUMMARY

The Convective Storm Initiation Project (CSIP) pilot field programme took place in the summer of 2004 in southern England. During this field campaign a case of a cold-pool outflow initiating an arc of convection downwind of the generating storm (the ‘primary storm’) was observed. Three further arcs were initiated further downwind of this first arc. These arcs all later gave significant rainfall over south-east England. Results from the modelling studies described in this paper show that gravity waves, generated by the ‘primary storm’, may have been responsible for initiating the further three arcs of convective showers that were observed.

The modelled primary storm generates waves with a range of vertical wavelengths. These are separated by dispersion, with the higher-order modes (with the largest vertical wavelengths) travelling fastest (approximately  $30 \text{ m s}^{-1}$ ). The fastest two modes suppressed convection and later modes increased boundary-layer depth and so initiated convection. The multiple peaks (from non-hydrostatic effects) in the third mode may have been responsible for the two main arcs observed and the fourth mode may have been responsible for the third arc. The amplitude of the modelled waves at low levels was much larger downwind of the primary storm than upwind and only initiated convection there, which agrees with the observations of the arcs forming downwind of the primary storm. This asymmetry appears to be caused by the moving-wave source and asymmetric wave trapping. Finally we discuss the implications for numerical weather prediction (NWP). Reducing the resolution of the model, and varying the magnitude of the wind speed used, shows that a non-hydrostatic high-resolution ( $\approx 1 \text{ km}$ ) NWP model should be able to capture such wave processes, if the generating storm is forecast or analysed correctly.

KEYWORDS: Cold pool Convection Gravity wave

### 1. INTRODUCTION

The Convective Storm Initiation Project (CSIP) aims to understand the processes that are responsible for the initiation of convection in the UK (i.e. a maritime midlatitude climate). This was motivated by the failure of current numerical weather-prediction (NWP) models to forecast the position and timing of the initiation of convection accurately, although they have skill in forecasting the likely regional location. This has serious implications for forecasting, especially of flooding, which is often caused by intense convective precipitation (for example the Boscastle storm on 16 August 2004). The main CSIP field campaign took place around the Chilbolton radar in the summer of 2005, with a pilot campaign in July 2004. This paper discusses a case-study from the pilot project.

CSIP aims to improve our understanding of both primary initiation (i.e. initiation of convective storm cells from perturbations in the boundary layer, which are not caused by existing storms) and secondary initiation (i.e. how existing convective cells can trigger new convection by modifying the atmosphere around them). This paper discusses only secondary initiation, in particular the role of cold pools and convectively generated gravity waves in the secondary initiation observed on 10 July 2004. An analysis of the observational data from this day is described in part I of this study (Morcrette *et al.* 2006).

Part I described the initiation of arcs of convection (called Arcs 1, 1a, 2 and 3) downwind (east) of an earlier storm (the ‘primary storm’) on 10 July 2004 (Figs. 3, 5 and 6 in part I). The ‘primary storm’ crossed the Bristol channel at approximately

\* Corresponding author: Institute for Atmospheric Science, School Earth and Environment, University of Leeds, Leeds LS2 9JT, UK. e-mail: jmarsham@env.leeds.ac.uk

0730 UTC and Arc 1 was initiated at around 0815 UTC approximately 30 km downwind (i.e. east) of the primary storm. Arcs 2 and 3 were initiated further downwind almost simultaneously at approximately 0845 UTC. Arc 1a was smaller than Arcs 1, 2 and 3 and developed between Arcs 1 and 2. Observations from the Chilbolton radar and surface observations show that Arc 1 was initiated by the cold-pool outflow from the primary storm, whilst Arcs 2 and 3 were not. Modulations in the boundary-layer height, observed using the clear-air radar at Chilbolton, preceded the formation of clouds within Arcs 2 and 3 by at least one hour. Using profiles from the Met Office Unified Model (UM), part I showed that the convective inhibition (CIN) was very sensitive to a lifting of only 15 hPa on this day and concluded that gravity waves generated by the primary storm may have been responsible for the initiation of Arcs 2 and 3. This paper uses idealized modelling experiments to test the hypothesis that convectively generated gravity waves from the primary storm affected the subsequent convection and to investigate:

- (i) why arcs were initiated preferentially on the downwind side of the storm,
- (ii) what controlled the spacing of these arcs, and
- (iii) how predictable was this process.

The simulations also capture the secondary initiation by the cold pool from the primary storm.

It is well known that gravity waves generated by a variety of sources (e.g. topography or upper-level jets, as well as convective storms) can influence convective activity (Einaudi *et al.* 1978) and Erickson and Whitney (1973) noted the effects of convectively generated waves not only on upper-level clouds, but also on low-level stratus. There have, however, been relatively few observational studies showing secondary initiation by convectively generated gravity waves from isolated storms. Shige and Satomura (2001) showed that ducted convectively generated waves were responsible for the initiation of new convection upwind of existing convective bands during TOGA COARE\*. Lac *et al.* (2002) also showed that convectively generated gravity waves had significant effects on convection during TOGA COARE by examining the auto-correlation function of deep convection in time and space. In addition, Lac *et al.* (2002) discussed a particular case where a wave mode (the  $n = 2$  mode) favours shallow convection and inhibits deep convection. Johnson *et al.* (1995) suggested that subsidence from convectively generated gravity waves were responsible for maintaining a gap observed between two mesoscale convective systems (MCSs), and McAnelly and Cotton (1997) also discussed the roles played by gravity waves in an MCS.

The uplift and latent heating from a convective storm tends to generate a fast deep wave mode, which gives compensating subsidence (e.g. Bretherton and Smolarkiewicz 1989; Nicholls *et al.* 1991). This mode, which has a vertical wavelength twice the depth of the troposphere, is referred to as the  $n = 1$  mode. Higher-order modes are also generated, but travel slower since they have smaller vertical wavelengths (e.g. the  $n = 2$  mode and  $n = 3$  mode have vertical wavelengths equal to the depth of the troposphere and two-thirds of the depth of the troposphere, respectively). Mapes (1993) showed that such modes could displace low-level parcels upwards, reducing CIN and so affecting the initiation and organization of subsequent convection. More recent modelling studies have investigated this mechanism further, although interestingly they differ in exactly which mode provides the low-level uplift. (e.g. Lac *et al.* (2002), Liu and Moncrieff (2004) and Nicholls and Pielke (2000) show this is provided by the  $n = 2$  mode, whereas Lane and Reeder (2001) show low-level subsidence from the  $n = 2$  mode and uplift

\* Tropical Ocean–Global Atmosphere; Coupled Ocean–Atmosphere Response Experiment.

from the slower  $n = 3$  mode.) In particular, Lane and Reeder (2001) discuss the effects of the gravity waves generated by a single convective storm on the CIN and Convective Available Potential Energy (CAPE) of the local environment. Lane and Reeder (2001) used an idealized profile, with zero mean wind. Wind shear can significantly affect the propagation of gravity waves (e.g. from trapping (Scorer 1949), or from wave dissipation at a critical level (Lindzen and Tung 1976)). Indeed, Nicholls and Pielke (2000) noted a pronounced asymmetry using a constant shear, with a stronger  $n = 2$  mode on the upshear side of the generating storm. Shear may also affect the generation of waves. The temporal variations in the diabatic heating within the cloud, oscillations of air parcels about their level of neutral buoyancy, and the so-called ‘obstacle effect’ (where updraughts in the cloud block the sheared horizontal flow and so generate waves in a similar manner to topography) all appear to contribute to the generation of gravity waves by convective storms (Lane and Reeder 2001) and shear will affect some, or all, of these processes. Parker and Burton (2002) also showed that if the speed of the source is comparable to the speed of the waves generated, the wave response is larger on the downwind side of the source.

In this paper we follow a similar method to Lane and Reeder (2001), using a warm bubble to initiate a convective storm in a cloud-resolving model. However, rather than using an idealized zero-shear profile, we use observed and modelled profiles, which include shear. A three-dimensional (3D) simulation was also performed in addition to 2D model runs. By adding surface fluxes, we also explore the influence of the gravity waves on the development of subsequent convection and compare the modelled results with observations from part I. Section 2 describes the model used and section 3 presents the results, both with and without surface fluxes. The results are discussed in section 4 and conclusions are summarized in section 5.

## 2. THE MODEL AND METHOD

All numerical simulations in this paper made use of the Met Office large-eddy model (LEM), a non-hydrostatic model (Gray *et al.* 2001). A non-hydrostatic model is required to capture non-hydrostatic dispersion, which can weaken the intensity of the convectively generated waves and can lead to multiple extrema trailing the leading edge of the disturbances (Pandya *et al.* 1993). The model was run with only warm-phase microphysics (Lane and Reeder 2001). The model had periodic lateral boundary conditions and a non-slip boundary condition at its bottom boundary. Rayleigh damping was applied between 13 km and the model top at 20 km to damp the gravity waves. Varying the height and strength of this damping layer had little effect on the simulations. High-resolution 2D simulations were used to capture the fine-scale structure of the waves generated and the secondary initiation process. For these simulations, we used a large domain of 1000 km to minimize the effects of the periodic lateral boundary conditions. (There were negligible differences between our standard runs and runs with double this domain size.) The model grid spacing was 200 m in the horizontal and approximately 100 m in the vertical (varying between 60 m at the surface and 200 m at 8 km). This adequately resolves both the generation and the propagation of the waves (Lane and Knievel 2005) as well as the convective-scale processes. In addition, results from a 3D simulation were compared with results from the 2D model runs. Computational constraints meant that this 3D run used a reduced domain size of 500 km  $\times$  500 km and a horizontal grid spacing of 4 km. The vertical grid of the experimental 1 km UM was used (as described in section 3(d)); this corresponds to a vertical grid spacing of approximately 400 m at 2 km. Results in section 3(d) show that,

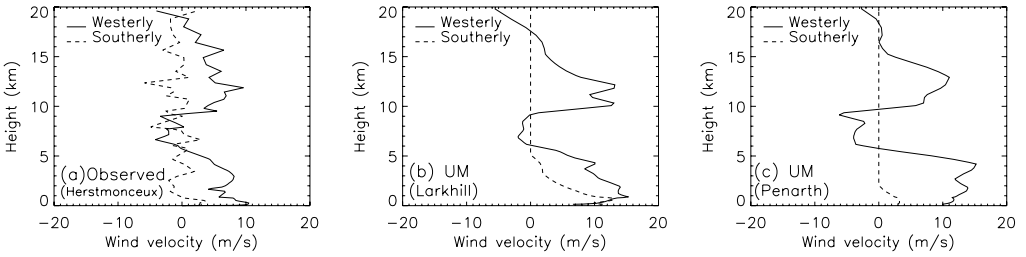


Figure 1. Wind profiles from (a) the Herstmonceux radiosonde at 11 UTC, (b) the Unified Model for Larkhill at 09 UTC and (c) the Unified Model for Penarth at 07 UTC.

although we expect this resolution to capture the basic effects of the ‘primary storm’ on the storm’s surroundings, the model is not expected to capture the finer-scale variations, which occur on scales of approximately 10 km.

We initialized the LEM using either a radiosonde sounding, or a profile from the Met Office UM. We generated a precipitating storm, to represent the observed ‘primary storm’, by adding a warm saturated bubble. This bubble, which consisted of an ellipsoidal potential temperature perturbation of 5.0 K, was added at the origin at the start of the simulation at a height of 1750 m and had horizontal and vertical axes of 8 km and 1500 m. This produced a precipitating cloud, approximately 25 km in diameter and with a cloud-top height of 6 km, comparable with the observed ‘primary storm’ (part I). Lane and Reeder (2001) showed that waves generated from such a ‘warm-bubble storm’ gave very similar gravity-wave structures (and so effects on CAPE and CIN) as storms generated by an isolated heating source.

Figure 1 shows winds from a radiosonde profile and the UM. Unfortunately radiosonde observations were not available from Larkhill (the nearest radiosonde site to the initiation of the arcs). So, an 11 UTC radiosonde profile from Herstmonceux ( $\approx 100$  km away) was used, as well as profiles from the UM, corresponding to the location of the initiation of the arcs (Larkhill) and the generation of the primary storm (Penarth). All profiles show moderate westerlies ( $\approx 10$  m s $^{-1}$ ) below approximately 5 km and above 8 km, with weaker easterlies between these levels. For the 2D simulations, the observed, or modelled, 3D wind profile was projected in an east–west or north–south direction. Results were similar whichever profile was used and results using the 11 UTC Herstmonceux radiosonde are used for the remainder of this paper.

### 3. RESULTS

Section 3(a) examines the waves generated by the warm-bubble storm in the LEM and their effects on CIN. Section 3(b) discusses the asymmetry of the waves in the up- and downwind directions. Section 3(c) describes the secondary initiation in the LEM, when surface fluxes are added to the model. Finally, section 3(d) discusses further sensitivities to the wind speed and model resolution. These are important for numerical weather prediction and also for understanding the differences between the 2D simulations run at a high resolution and the lower-resolution 3D model runs.

#### (a) Waves generated and their effects on Convective Inhibition

The high-resolution 2D model was run using three different wind profiles: the observed westerly wind, the observed southerly wind and no wind. The lower-resolution 3D model was run using the observed wind profile. We first consider the 2D simulations.

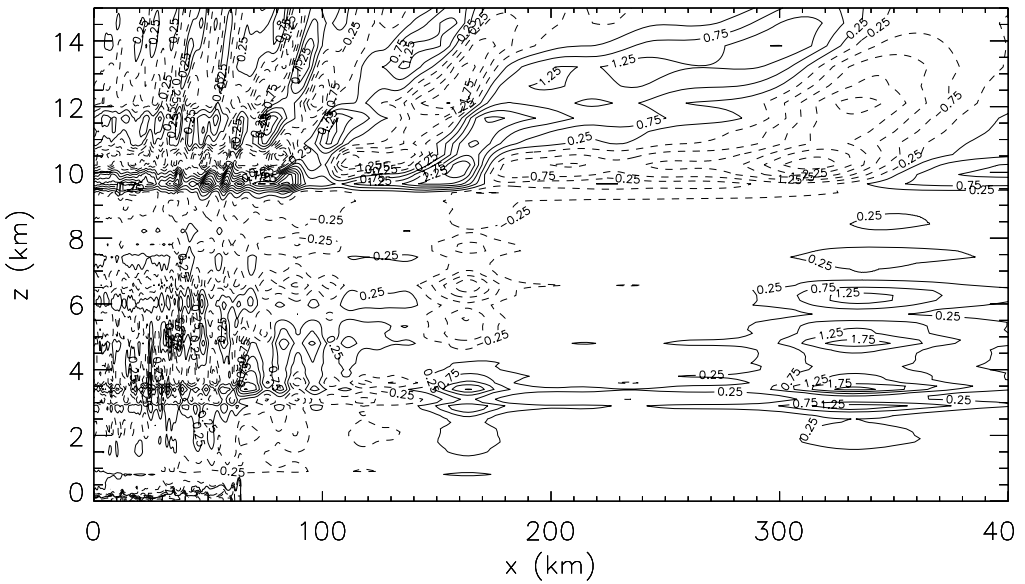


Figure 2. Cross-section of potential temperature perturbations at three hours with no wind. Contours are shown at  $\pm 0.25$  K and at 0.5 K intervals, with solid and dashed lines showing positive and negative values. The cold pool is denoted by a bolder solid line (water vapour mixing ratio  $> 6.0$  g  $\text{kg}^{-1}$ ). The primary storm, which was initiated at  $x = 0$  has almost completely dissipated by this time.

In the no-wind case (Fig. 2) the potential temperature perturbations are, as expected, symmetric about  $x = 0$ . The  $n = 1$ ,  $n = 2$  and  $n = 3$  modes (Lane and Reeder 2001) are at approximately  $x = 340$ , 160 and 90 km respectively. The multiple extrema, caused by non-hydrostatic dispersion (Pandya *et al.* 1993), can be seen for some of the same modes (this is clearest at  $x = 80$  to 120 km for the  $n = 3$  mode). The  $n = 1$  mode has little effect on the boundary layer (since its maximum amplitude occurs at a height of approximately 4 km). Figure 3 shows that the  $n = 2$  mode (at  $x \simeq 160$  km) decreases the boundary-layer height and the  $n = 3$  mode (at  $x \simeq 90$  km) increases it (as observed by Lane and Reeder 2001). The lifting of the top of the boundary layer by the cold pool can be seen at approximately  $x = 65$  km, as well as oscillations in boundary-layer height from the higher-order modes behind this.

The westerly wind has significant effects on the modelled waves (Fig. 4). The  $n = 1$  mode can be seen at  $x = 350$  and  $-300$  km. The  $n = 2$  mode (at  $x = 210$  and  $-140$  km) affects lower levels more strongly on the downwind side ( $x > 0$ ). The  $n = 3$  mode (at  $x = 150$  and  $-50$  km) is much stronger on the downwind side, particularly at lower levels. The cold pool is also asymmetric, with a deeper head downwind of the generating storm. In comparison, the weak southerly wind (Fig. 1) has little effect on the potential temperature perturbations at three hours compared with the no-wind case (not shown, but Fig. 5 shows that the convective inhibition at the lowest model level at three hours is almost symmetric about the ‘primary storm’ for the southerly wind case). The reasons for these asymmetries in the waves are discussed in section 3(b).

The cold pool and wave structures generated in the 3D model were similar to those in the 2D model, although as expected the wave amplitudes decayed more quickly in 3D as they propagated away from ‘primary storm’ and the cold-pool outflow is slower (since the storm is essentially a point source in 3D and an infinite line source in 2D).

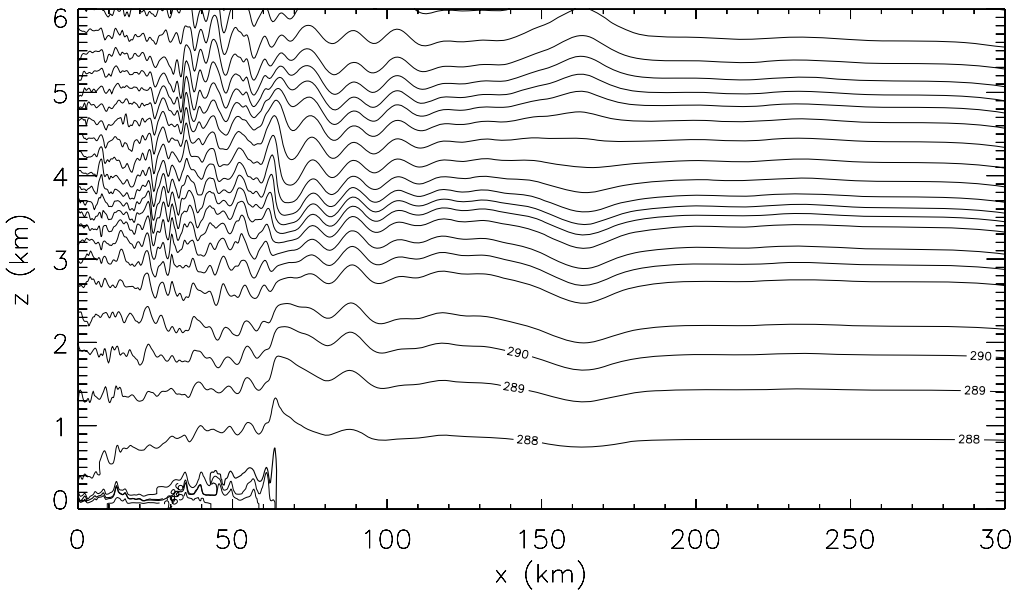


Figure 3. Cross-section of potential temperature (K, contours) at three hours with no wind. The cold pool is denoted by a bolder solid line (water vapour mixing ratio  $> 6.0 \text{ g kg}^{-1}$ ).

In addition the lower resolution used in the 3D simulation (i.e. a 4 km grid spacing rather than a 200 m grid spacing) introduces some differences between the 2D and 3D results:

- (i) the horizontal wave speeds are slightly slower ( $\approx 6\%$ ) in 3D, and
- (ii) the multiple peaks from non-hydrostatic effects are also less clear in the 3D runs.

These resolution effects are discussed in section 3(d).

CIN is the amount of work required to lift air from a given height to its level of free convection. All runs showed increases in CIN from the  $n = 1$  and  $n = 2$  modes (which decrease the boundary-layer depth) followed by decreases in CIN from the  $n = 3$  mode (which increases the boundary-layer depth). Figure 5 show CIN at the lowest model level in the 2D and 3D simulations at three hours. As expected, the amplitude of the waves decays more quickly in the 3D model than the 2D model, but the speeds of the waves are similar. The cold pool also propagates more slowly in the 3D case, as expected. Figure 5 shows that using the observed southerly wind introduces little asymmetry into the CIN cross-section, in either 2D or 3D, but does give slightly larger wave effects on the northern ( $x > 0$ ) side of the storm. The minimum in CIN at the edge of the cold pool is slightly deeper on the southern side ( $x = -60 \text{ km}$  in 2D). The observed westerly wind leads to a much more significant asymmetry in the cross-section of CIN. The effects of the cold-pool  $n = 2$ ,  $n = 3$ , and  $n = 4$  modes are all much larger on the downwind side of the generating storm (in both 2D and 3D). The higher-resolution 2D simulations also show that oscillations in CIN from the  $n = 4$  mode propagate significantly faster than the cold-pool outflow, when the observed westerly wind is used. Removing the rain, and so the cold pool, from the LEM showed these multi-modal structures (which were well resolved by the model's 200 m grid spacing) were not generated by the cold-pool outflow from the storm. Furthermore, smoothing the potential temperature and wind profiles also showed that the multi-modal waves were not caused by unrealistically sharp gradients in the profiles. Further sensitivity tests showed that the magnitudes of the effects of the

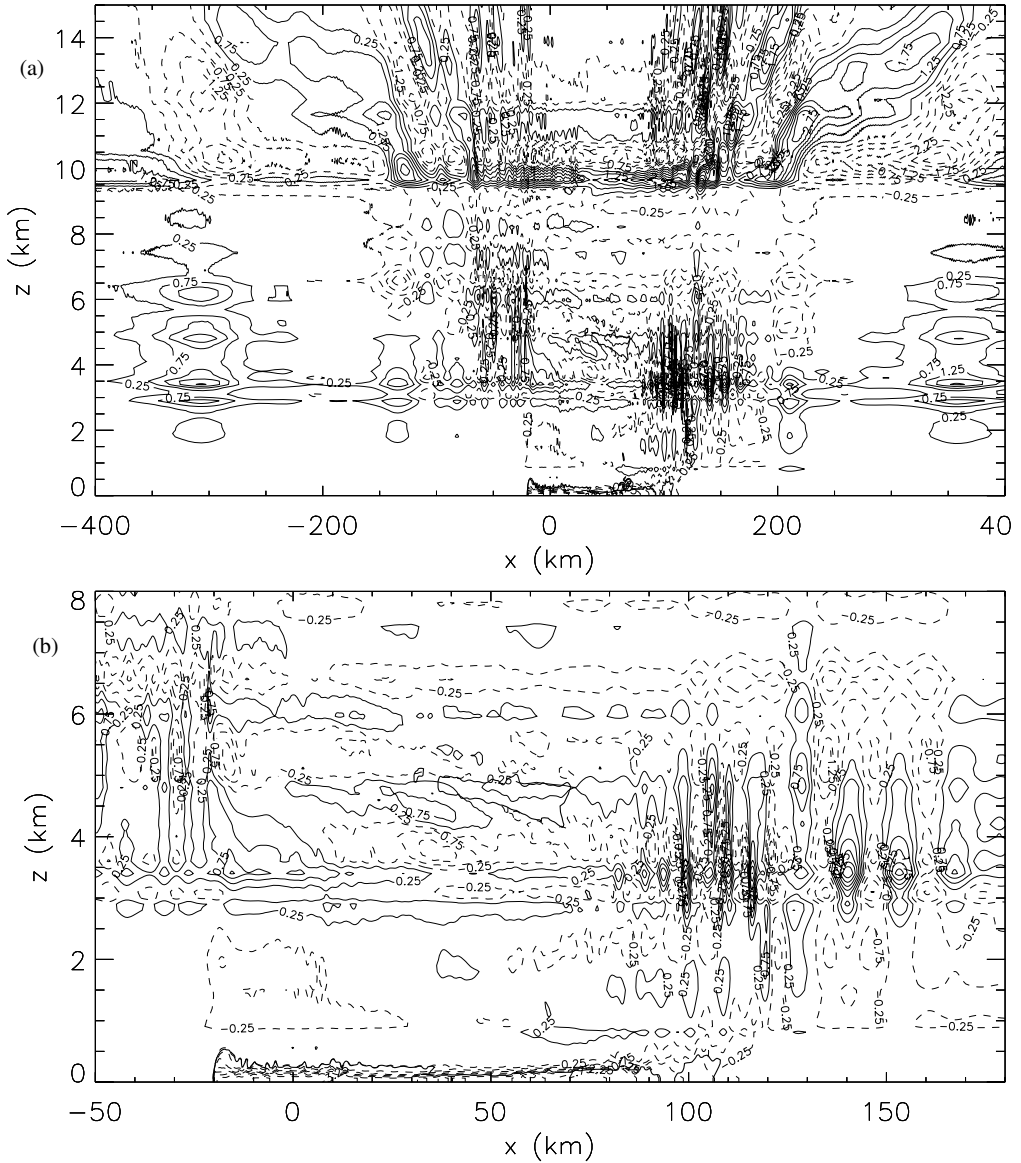


Figure 4. (a) is as Fig. 2, but with the observed westerly wind and different horizontal scale. (b) shows data from a more limited area, in order to show the higher-order wave modes more clearly. In both panels, the remnants of the parent storm (liquid water mixing ratio  $> 0.25 \text{ g kg}^{-1}$ ) are shown by a bolder solid line.

convectively generated waves in the LEM were sensitive to the the size and temperature perturbation of the initial ‘warm bubble’. However, the wave speeds were not and the wind-induced asymmetries always occurred.

Figure 6 shows CIN at the surface three hours after the initiation of a storm in the 3D simulation. The effects of the  $n = 2$  mode are apparent in a circle around the storm, whereas the  $n = 3$  mode is much clearer on the downwind side ( $x > 0$ ). The broad arc of lowered CIN on the downwind side (which is more clearly dual-peaked in the high-resolution 2D runs) is reminiscent of the arcs of convection shown downwind of the

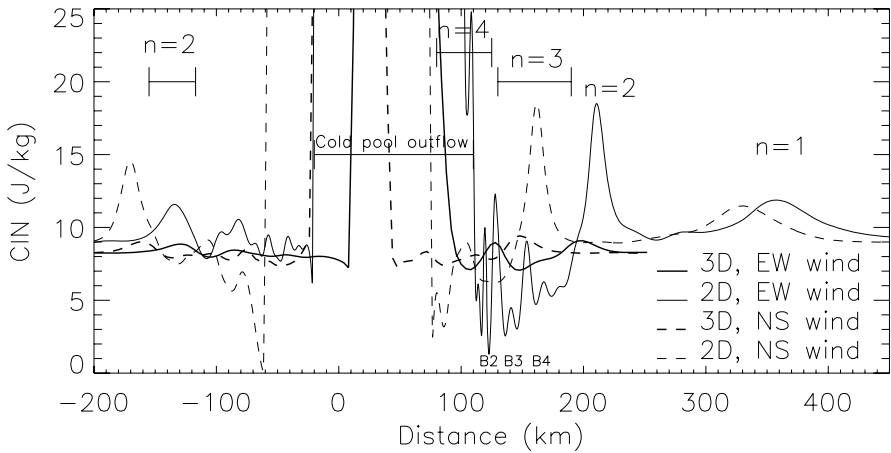


Figure 5. Convective inhibition (CIN) at 3 hours using the 11 UTC Herstmonceux radiosonde profile.  $n = 1$ ,  $n = 2$  etc. refer to the 2D westerly wind case. B2, B3 and B4 show the minima in CIN responsible for initiating the cells of convection in the 2D run using the westerly wind and surface fluxes (section 3(c), Fig. 15).

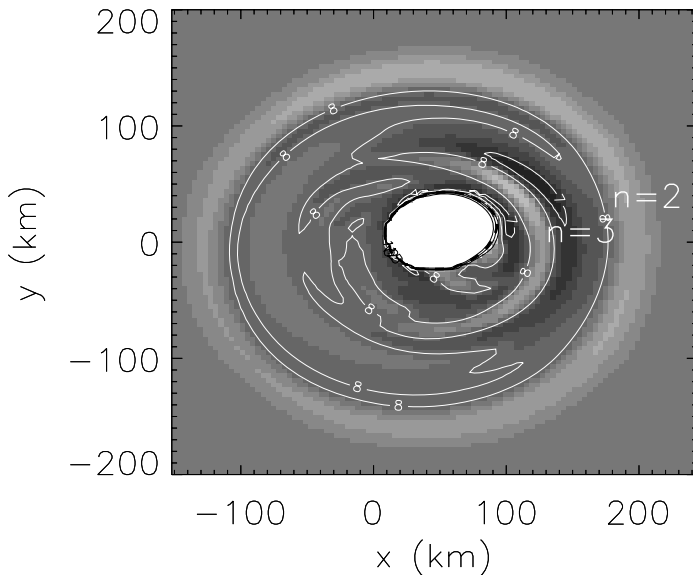


Figure 6. Convective inhibition ( $\text{J kg}^{-1}$ ) at the surface after 3 hours in the 3D simulation (horizontal grid spacing equals 4 km). The bold dashed line indicates the edge of the cold pool.

primary storm in Figs. 5 and 6 of part I. We conclude that on 10 July 2004 convectively generated gravity waves could have led to significant low-level perturbations downwind of any major convective storms. This upwind/downwind asymmetry agrees with the observations of the arcs being initiated downwind of the ‘primary storm’ (part I). If Arcs 2 and 3 were initiated by convectively generated gravity waves, then we can understand this asymmetry in terms of the wind-shear profile, rather than topographic or land/sea differences. The reasons for this modelled asymmetry are discussed in section 3(b).

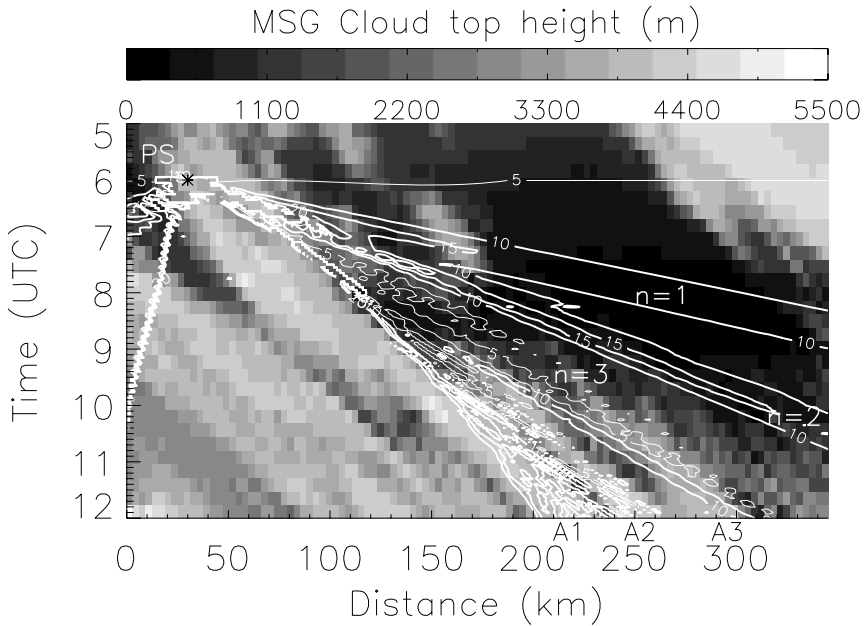


Figure 7. Contours of convective inhibition (CIN) (from the high-resolution 2D LEM simulation, using the 11 UTC Herstmonceux radiosonde profile and the observed westerly wind component) superimposed on a grey-scaled Hovmüller plot of cloud-top heights derived from MSG (part I). The asterisk (\*) shows the original centre of the ‘warm-bubble storm’ added to the LEM at  $t = 0$ . The changes in CIN appear slightly discontinuous because they have been generated from LEM diagnostic output every 7.5 minutes, whereas in reality they are continuous. A1, A2, A3 and PS refer to the observed arcs and the primary storm.  $n = 1$ ,  $n = 2$  and  $n = 3$  refer to the wave modes generated by the primary storm in the LEM.

We now relate the modelled wave speeds to observations available from 10 July 2004. Figure 7 shows a space–time (i.e. Hovmüller) plot of CIN from the LEM superimposed on a Hovmüller of cloud-top height calculated from Meteosat-8 (from part I). The positioning of the LEM storm on the observed data is clearly subjective, but the results are robust to the exact location within the observed primary storm. The  $n = 1$  and  $n = 2$  modes clearly correspond to largely cloud-free regions (and even appear to suppress existing clouds at 160 km at 0730 UTC). Arcs 2 and 3 initiate as the CIN decreases as the  $n = 3$  mode approaches. These results suggest that waves generated by the primary storm could be significant in the suppression of convection downwind of the primary storm and the subsequent initiation of the arcs of convection observed. They also suggest that the multiple minima in CIN shown in Fig. 5 may be related to the two main arcs of convection that were not initiated by the cold-pool outflow (Arcs 2 and 3, part I). The speed of each peak in the  $n = 3$  mode also corresponds well to the speed of the onset of precipitation shown in part I, Fig. 8. These ideas are investigated in section 3(c), where surface fluxes were added to the LEM to allow secondary convective initiation to occur in the model and are discussed in section 4.

(b) *The asymmetry of the gravity waves*

Parker and Burton (2002) show that gravity waves are generated asymmetrically by a heat source if the speed of a wave source is comparable with the speed of the waves. This is expected to occur in this case, since the primary storm moves at  $\approx 6 \text{ m s}^{-1}$  and the phase speeds of the  $n = 2$  and  $n = 3$  waves, relative to the air, are approximately

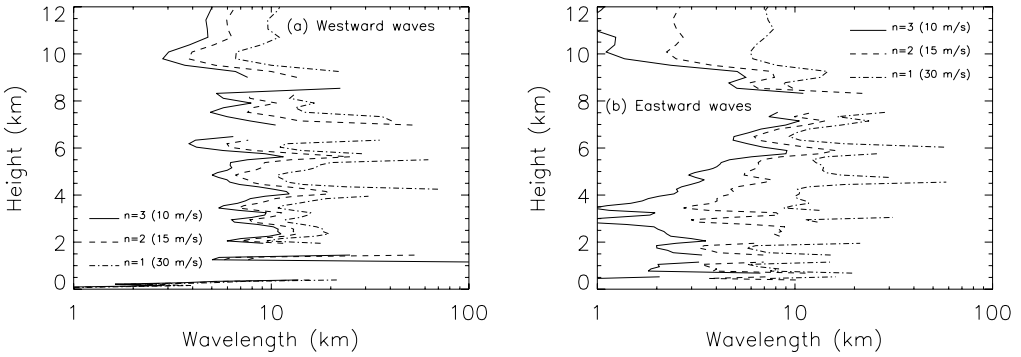


Figure 8. Profiles of the horizontal wavelengths of (a) westward and (b) eastward waves corresponding to the Scorer parameter for the 11 UTC Herstmonceux radiosonde profile. (We expect trapping for wavelengths smaller than the values shown.) Lines are shown for three phase velocities, corresponding to the  $n = 1, 2$  and 3 modes.

$15 \text{ m s}^{-1}$  and  $10 \text{ m s}^{-1}$ . We also expect the wind profile to influence the propagation of gravity waves. The Taylor–Goldstein equation (Taylor 1931; Goldstein 1931) states

$$\frac{\partial^2 w}{\partial z^2} + \left\{ \frac{\bar{u}_{zz}}{(c - \bar{u})} + \frac{N^2}{(c - \bar{u})^2} - k^2 \right\} w = 0, \quad (1)$$

where  $z$  is height,  $w(z)$  is the vertical air velocity,  $\bar{u}(z)$  is the basic state wind velocity,  $N$  is the Brunt–Väisälä frequency and  $c$  and  $k$  are the phase velocity and horizontal wave number. The subscript  $_{zz}$  denotes  $d^2/dz^2$ . The first two bracketed terms in (1) are called the Scorer parameter,  $\lambda^2$ , defined by

$$\lambda^2(z) = \frac{\bar{u}_{zz}}{(c - \bar{u})} + \frac{N^2}{(c - \bar{u})^2}. \quad (2)$$

If  $\lambda^2 - k^2$  is positive then  $w(z)$  can have an oscillatory solution; if  $\lambda^2 - k^2$  is negative then  $w(z)$  will decay exponentially with height, i.e. if the Scorer parameter is  $< k^2$ , this will tend to give wave trapping. Crook (1988a) shows that winds opposing the waves at upper levels can increase the magnitude of  $|c - \bar{u}|$ , increasing wave trapping, so Fig. 1 shows that we might expect some trapping for eastward-propagating waves in this case. Crook (1988b) shows that a jet in the stable layer opposing the wave motion can also lead to wave trapping, since the reverse curvature in the wind profile then reduces the Scorer parameter. Additionally, an inversion at upper levels can reflect wave energy, giving large wave amplitudes at low levels. Maximum reflection occurs if both the layer below the inversion and also the inversion itself are one quarter of a vertical wavelength deep (Crook 1988b).

Figure 8(a) shows that for waves propagating from east to west, against the low-level wind, the trapping effects are relatively constant with height and the Scorer parameter is largely negative below 2 km. In contrast, for waves propagating from west to east, with the low-level wind, the trapping increases with height and the Scorer parameter is largely positive below 2 km (Fig. 8(b)). For eastward waves with a phase speed of  $10 \text{ m s}^{-1}$  (the  $n = 3$  mode), this corresponds to some trapping for wavelengths less than 1 km at a height of 3 km, wavelengths less than 11 km at 5.8 km and all wavelengths at 7.5 km. This increase in trapping with height is caused by the opposing winds above 6 km (Fig. 1) and the decrease of the Brunt–Väisälä frequency with height (Fig. 9). So, it is possible that upward propagation of waves travelling eastwards is

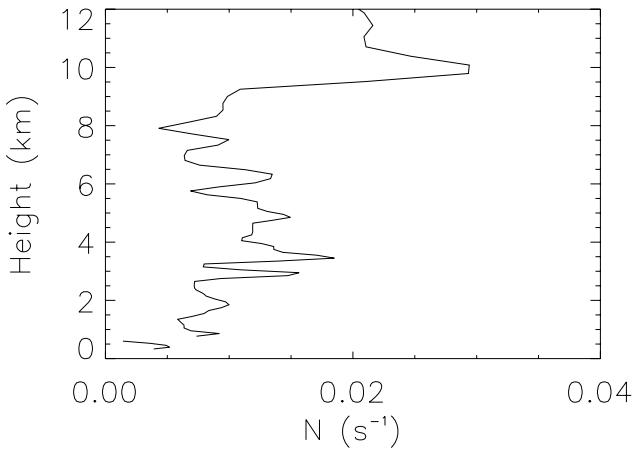


Figure 9. The Brunt-Väisälä frequency,  $N$ , as a function of height.

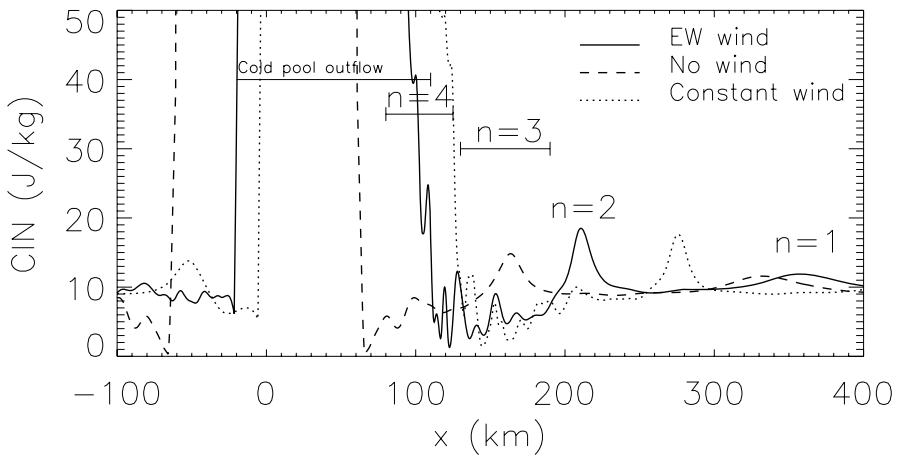


Figure 10. As Fig. 5, but for 2D runs using: no wind (dashed), a constant wind of  $10 \text{ m s}^{-1}$  decreasing to zero below 300 m (dotted), and the observed westerly wind (solid).

inhibited by the decrease in Scorer parameter with height, whilst for waves propagating westwards amplitudes decay below 2 km to  $w = 0$  at  $z = 0$ , since the Scorer parameter is negative below this level. This hypothesis is consistent with the modelled wave amplitudes, which are much larger downwind of the primary storm than upwind at a height of 1 km, and decrease rapidly with height above approximately 5 km on the downwind side (Fig. 4).

Figure 10 shows the effects of using a constant westerly wind (of  $10 \text{ m s}^{-1}$ ) above 300 m (with the wind speed decreasing to zero below 300 m). Again we see an asymmetry with the waves affecting CIN much more downwind than upwind, even without the opposing winds at upper levels, although in this case there are also more significant effects from the  $n = 2$  and  $n = 3$  modes upwind of the primary storm. This suggests that there may be some wave trapping by the opposing upper-level flow, but that much of the asymmetry may be from the moving wave source (Parker and Burton 2002).

When the potential temperature profile was smoothed, the low-level perturbations in CIN were relatively unaffected, which suggests that reflection from lids (e.g. at 3.2 and 3.8 km, Fig. 9) is not significant in this case, since such reflections are sensitive to the fine-scale structure of the profile. Wave ducting (Lindzen and Tung 1976; Wang and Li 1999) requires a critical layer, where the wind velocity is equal to the wave's horizontal phase velocity. In this case the wind speed is not large enough to give significant ducting for the  $n = 2$ ,  $n = 3$  or  $n = 4$  modes, which have phase speeds of approximately 15, 10 and  $7.5 \text{ m s}^{-1}$  respectively (Fig. 1). As a result it seems the asymmetry in the low-level wave amplitudes is caused by the moving wave source (Parker and Burton 2002) and possibly some wave trapping. This trapping is caused by the easterly upper-level winds and Brunt–Väisälä frequency decreasing with height (Crook 1988b). Wave amplitudes are small upwind of the primary storm below a height of 2 km, since the Scorer parameter is largely negative for waves propagating westwards below this level.

### (c) *Secondary initiation*

Surface fluxes were added to the 2D simulations so new convective cells developed within the model (the 200 m grid spacing of the 2D simulations allowed reasonable resolution of the convective initiation). A sensible heat flux of  $80 \text{ W m}^{-2}$  and a latent heat flux of  $200 \text{ W m}^{-2}$  were used, since this allowed clouds to develop at approximately the same time in the LEM as in reality. Figures 11 and 12 show Hovmöller plots using the westerly wind and southerly wind respectively. Figure 13 shows the results from using the westerly wind, but with no warm-bubble primary storm. As expected, there are significant differences between the development of moist convection with the two different wind profiles and with/without the primary storm.

With the observed westerly wind and a warm-bubble primary storm, further convection developed in distinct cells, which are advected downwind (Fig. 11). Some of these are narrow, with liquid-water paths (LWPs) of 400 to  $800 \text{ g m}^{-2}$ , whilst those labelled B1 to B4 and C1 contain wider areas of deeper convection and LWPs up to  $1500 \text{ g m}^{-2}$ . Cells B3 and B4 have spacings similar to the arcs observed ( $\approx 35 \text{ km}$ , compared with  $\approx 45 \text{ km}$ ). Cells B1 and C1 are initiated by the cold-pool outflow from the primary storm (Fig. 14). Cell B1 is initiated before C1 since the head of the cold pool is deeper on the downwind side (Fig. 4). This is consistent with Moncrieff and Liu (1999), who show that the horizontal convergence and mean ascent at the head of a cold-pool outflow can be increased by it either propagating downwind or upshear, but that the head wind can outweigh the shear effect. There is more convective cloud downwind of B4 in the LEM than observed, but this is not surprising, since we are using the profile from 11 UTC in an idealized model experiment.

The run using the southerly wind gave more and narrower regions of moist convection, which did not persist (Fig. 12). The deepest clouds in this case formed at around  $x = 80 \text{ km}$  at approximately 08 UTC. These deeper clouds are again related to the cold-pool outflow from the primary storm. This agrees qualitatively with the observations, which suggest that convection was initiated by the cold pool in a circle around the primary storm, but it is deeper and more persistent on the downwind side (part I, Fig. 6). Using the observed westerly wind, but no primary storm (Fig. 13), again produced moist convection. However, without the primary storm this develops an hour later (despite random perturbations being added to the run to initiate convection) and almost simultaneously at all locations.

The observed Arc 1 and the modelled B1 were both initiated by the cold-pool outflow from the primary storm. The other deeper convective cells in the LEM appear to be initiated by, or at least influenced by, convectively generated gravity waves.

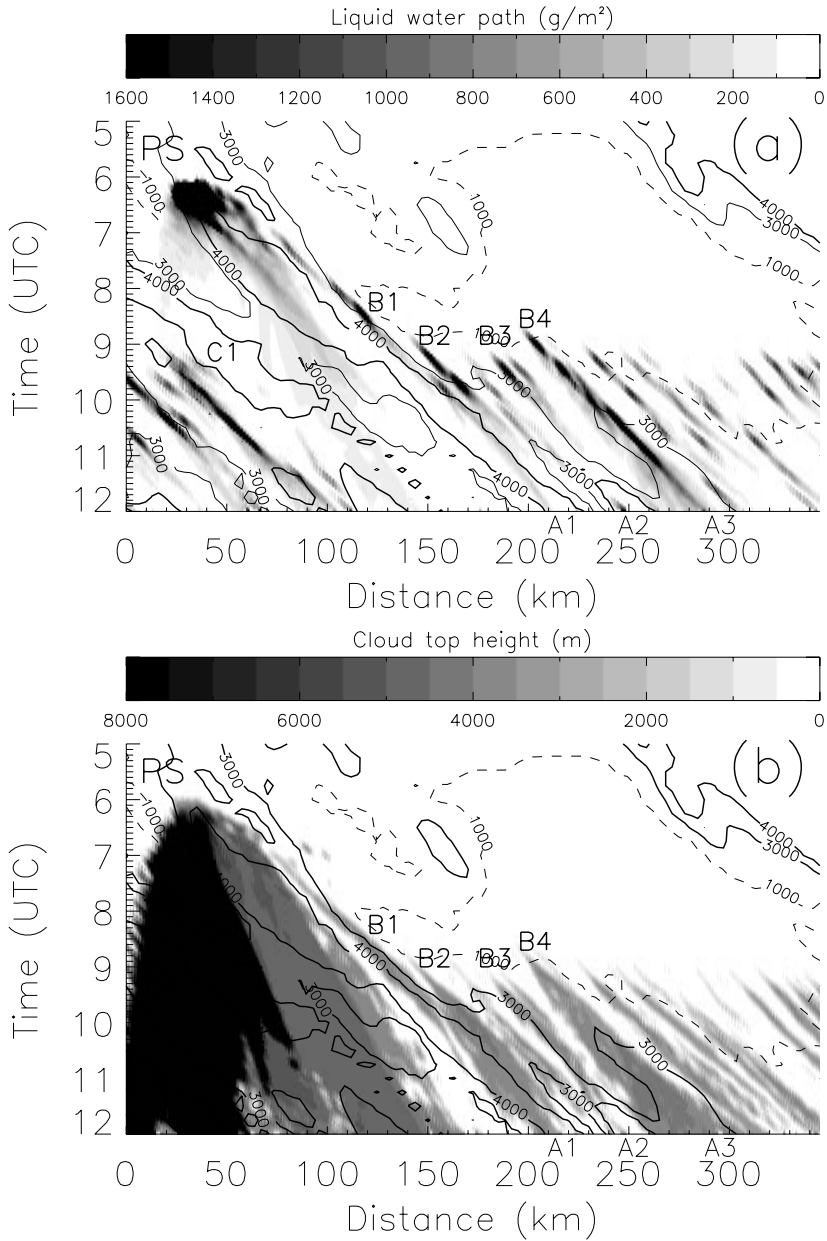


Figure 11. Hovmüller diagrams of (a) liquid water path ( $\text{g m}^{-2}$ , grey shading) and (b) cloud-top height (m, grey shading), both from the LEM. In both, contours of cloud-top height (m) derived from Meteosat-8 (part I) are superimposed. A1, A2, A3 and PS refer to the observed arcs and the primary storm. B1, B2, C1 etc. refer to the cells generated in the LEM.

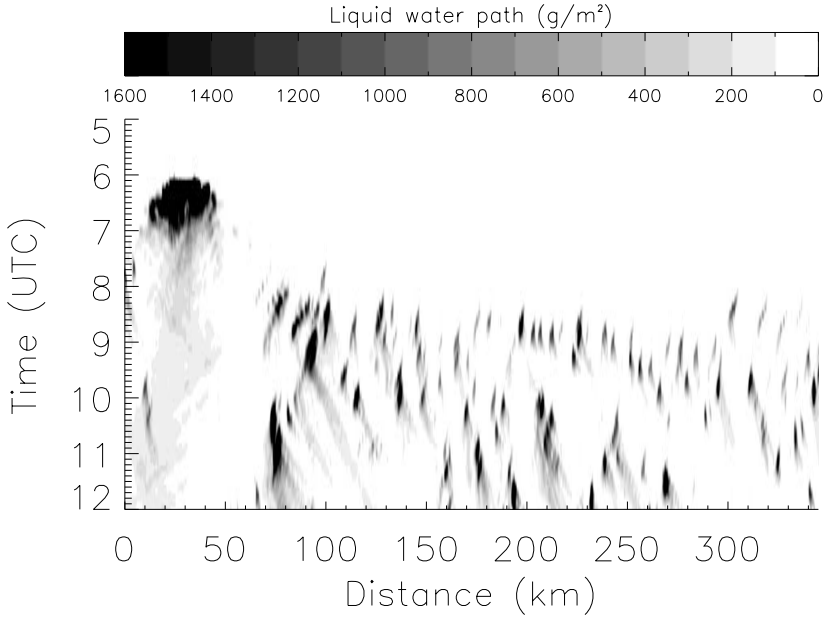


Figure 12. Hovmüller plot of liquid water path ( $\text{g m}^{-2}$ ) from the LEM, using the southerly component of the observed wind from the 11 UTC Herstmonceux radiosonde profile.

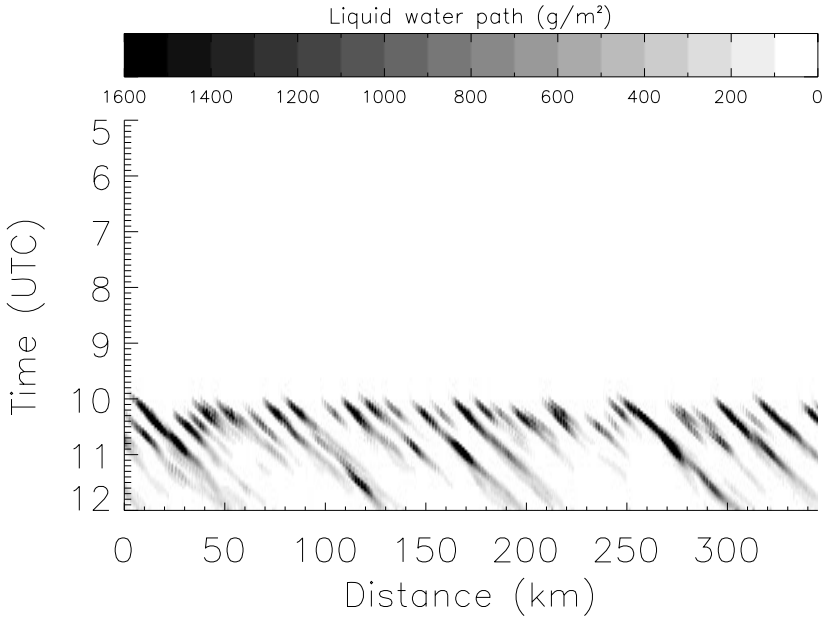


Figure 13. As Fig. 12, but using the westerly component of the observed wind and no primary storm.

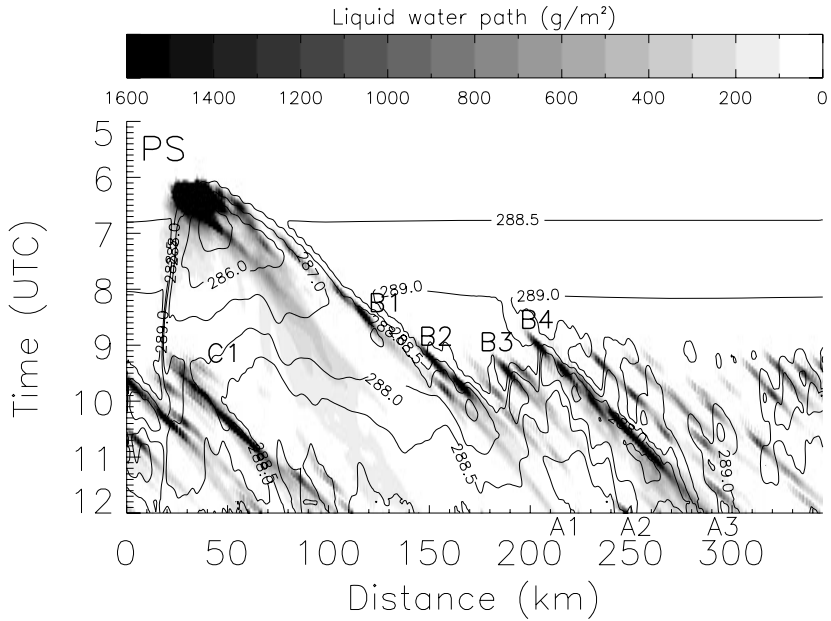


Figure 14. Hovmüller diagram of potential temperature at the surface in the LEM (K, contours), superimposed on liquid water path (shading). The run used the observed westerly wind profile.

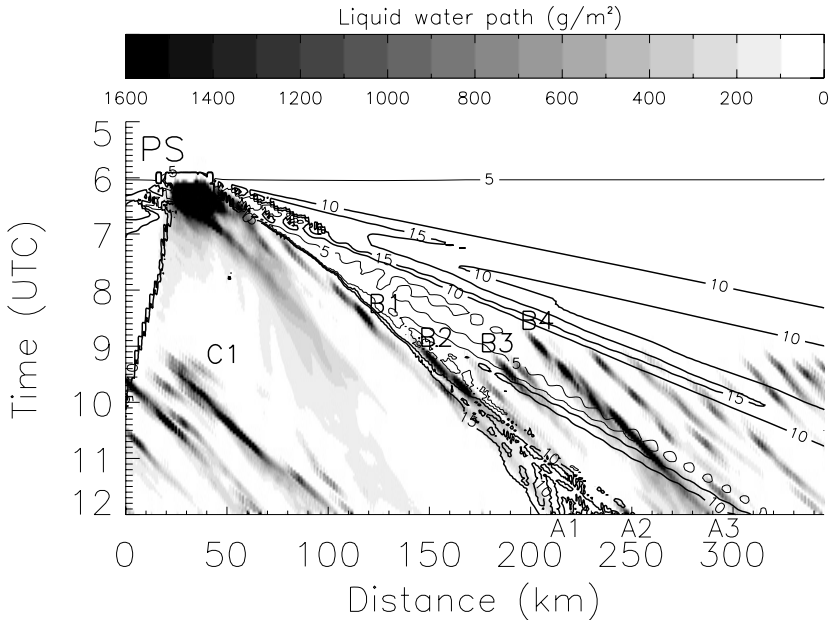


Figure 15. Hovmüller diagram of convective inhibition ( $\text{J kg}^{-1}$ , contours) from an LEM run with no surface fluxes, superimposed on liquid water path ( $\text{g m}^{-2}$ , shading) from an LEM run with surface fluxes.

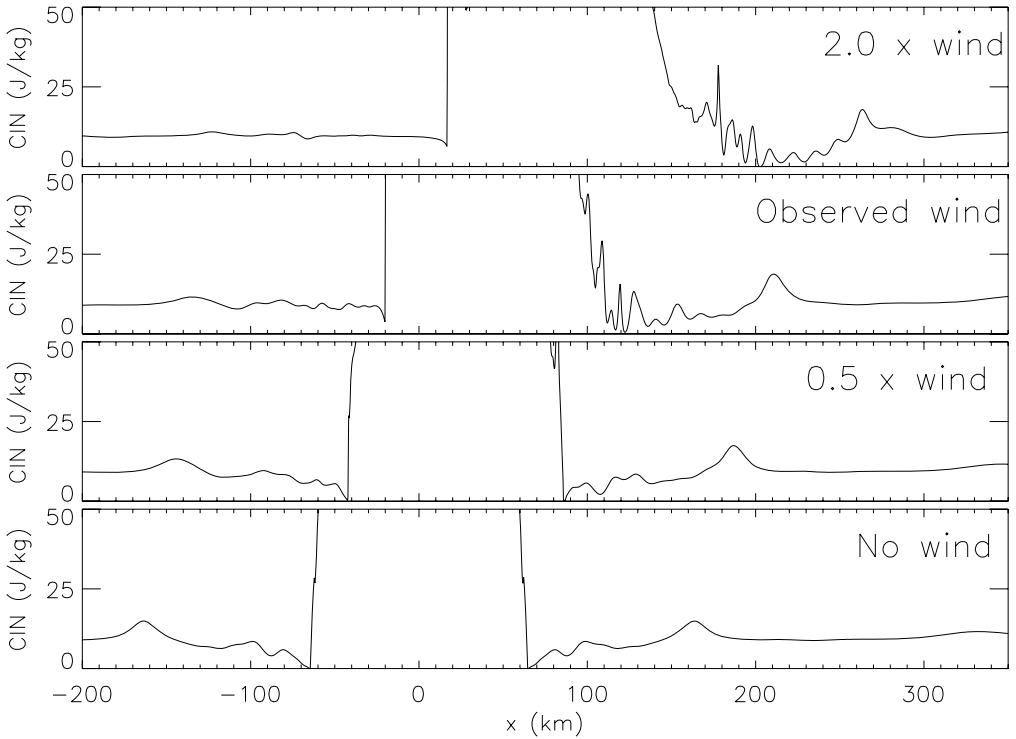


Figure 16. Effect of varying shear on convective inhibition. The wind speed was varied between 0 and 2 times the observed westerly wind.

Figure 15 shows that B3 and B4 are initiated by the two minima in CIN from the dual-peaked  $n = 3$  mode. (Approximately one hour later, B3 appears to be suppressed by a peak in CIN between the  $n = 3$  and  $n = 4$  modes.) B2 appears to have been initiated by the  $n = 4$  mode and the cold pool from the primary storm (Figs. 14 and 15). Since the moist convection in the arcs is initiated by decreases in CIN associated with waves that increase the depth of the boundary layer, an increase in boundary-layer height can be observed in the LEM before the clouds form. However, these perturbations travel at the speed of the relevant waves ( $\simeq 19$  and  $14 \text{ m s}^{-1}$  relative to the ground for the eastward-propagating  $n = 2$  and  $n = 3$  modes), which is faster than the modulations observed in the Chilbolton radar data in part I, which appear to move with the mean wind at  $\simeq 8 \text{ m s}^{-1}$  (part I, Fig. 18).

(d) *Sensitivities to the wind speed and model resolution*

Figure 16 shows how the CIN at the surface varies as the absolute wind speed is varied in 2D LEM simulations. The changes are continuous in nature for the three lower wind speeds used, with an increased wind deepening and widening the region of reduced CIN caused by the  $n = 3$  mode. The effect is much more significant for the strongest shear case. We can conclude that, although the wind profile is important for this event, the accuracy of this profile is unlikely to limit the forecasting of such a gravity-wave event.

The Met Office currently routinely runs the UM at a 4 km horizontal resolution for the UK, with an experimental 1 km resolution run for a limited area. This resolution is

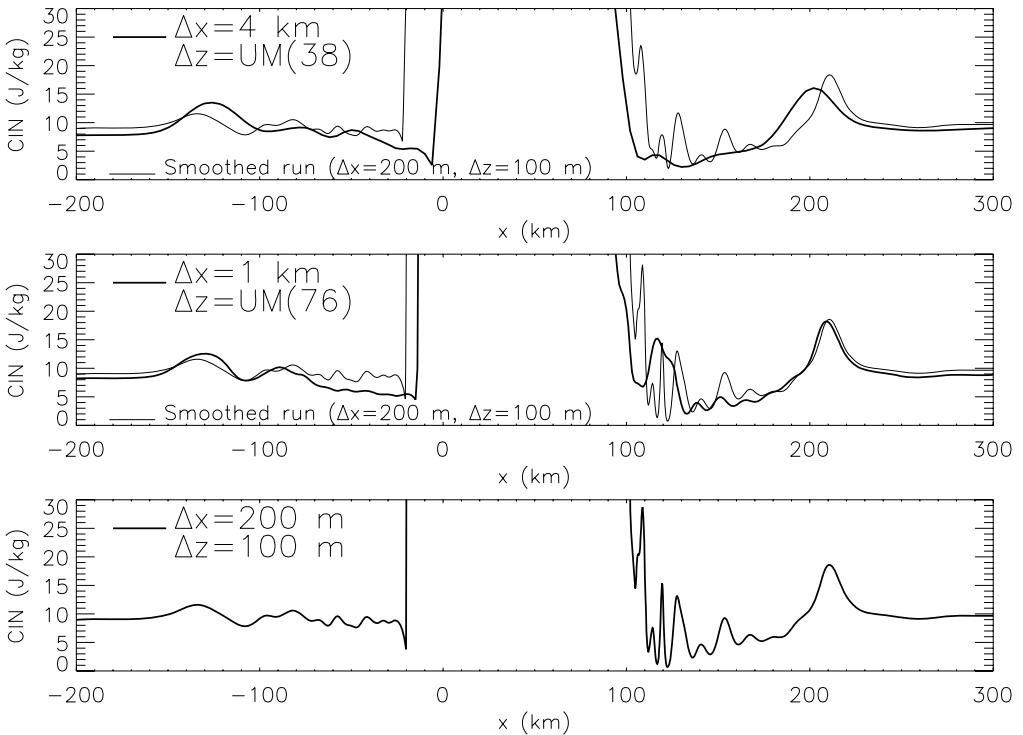


Figure 17. Convective inhibition (CIN) at three hours using various resolutions in the LEM. Bold lines show CIN from runs using the horizontal and vertical grid spacings  $\Delta x$  and  $\Delta z$ . The thin lines show the highest-resolution run ( $\Delta x = 200$  m) smoothed to the relevant horizontal grid spacing (i.e. 1 km or 4 km). UM(38) and UM(76) refer to the 38 and 76 model levels used in the Unified Model.

significantly lower than that used in the 2D LEM experiments presented in this paper (i.e. 200 m). Figure 17 shows the effects on the CIN of varying the resolution in the LEM. The horizontal resolution of 200 m was reduced to either 1 km or 4 km, and the vertical resolution was reduced to the 76 or 38 levels used in the UM (for the 1 km and 4 km runs respectively). Results from runs with poorer horizontal resolutions include significantly less fine-scale structure than the high-resolution run smoothed to the lower horizontal resolution, but do capture the basic shape of the CIN profile well. The speed of the  $n = 2$  mode is approximately 6% lower in the run using a 4 km grid spacing. This suggests that the difference in wave speeds in 2D and 3D for the  $n = 2$  mode (Fig. 5) is from the differences in resolution, rather than from 3D effects. The 1 km run gives a lower peak in CIN from the  $n = 2$  mode than the 200 m resolution run, but does capture the minimum in CIN from the  $n = 3$  mode. This suggests that if the current generation of NWP models forecast or analyse the primary storm correctly, they would capture the increased tendency for convection downwind of the primary storm. They would, however, be unlikely to capture all the details of the secondary convective structures.

#### 4. DISCUSSION

There is good agreement between (i) the observed timing of the onset of convection and the speed of the  $n = 2$  and  $n = 3$  modes (Fig. 7) and (ii) the modelled and observed asymmetries in the convective initiation (Fig. 5 and part I, Fig. 6). This strongly suggests

that the  $n = 1$  and  $n = 2$  modes inhibited convection downwind of the ‘primary storm’ until the  $n = 3$  mode initiated convection. Two peaks in the  $n = 3$  mode led to two local minima in CIN in the model and initiated cells B3 and B4 in the LEM (Figs. 5 and 15). These corresponded well with the observed Arcs 2 and 3 (Fig. 11) and it seems likely that two peaks in the  $n = 3$  mode initiated the Arcs 2 and 3 in reality. However, sensitivity studies using multiple warm bubbles suggest that it is also possible that Arcs 2 and 3 were initiated by two  $n = 3$  waves from the two initial cells of the ‘primary storm’ (part I, Fig. 5). The good agreement between the modelled  $n = 3$  wave and the observed onset of precipitation (Figs. 7 and part I, Fig. 9) also suggests that a single peak in the  $n = 3$  mode may have contributed to the deepening of the clouds in both Arcs 2 and 3. This could, however, be a coincidence and the slower onset of precipitation in Arc 3 compared with Arc 2 (part I, Fig. 8) may be because Arc 3 was initiated by a weaker peak in the  $n = 3$  mode (Fig. 5). In addition, it is also possible that the less-distinct Arc 1a was related to a higher-order wave. (Fig. 15 shows that the modelled  $n = 4$  mode, with the cold pool from the primary storm, initiated B2 in the LEM.) However, other mechanisms, such as multiple pulses from the primary storm, are possible. The model results are again consistent with the initiation of Arc 1 on the eastern (downwind) side of the cold pool generated by the primary storm, whereas the effects of the cold pool were much more limited to the west.

An array of microbarographs would allow the retrieval of the speeds of the waves from their observed surface pressure signals, and comparing modelled and observed wave speeds would allow a good test of the wave mechanisms proposed in this paper. Such an array of pressure sensors was, unfortunately, not available. However, the amplitudes of the pressure perturbations from the 3D LEM simulations (0.1 hPa, 0.06 hPa and 0.04 hPa for the  $n = 1, 2$  and  $3$  modes respectively) are consistent with the surface pressure perturbations observed at Facombe (part I, Fig. 12).

## 5. CONCLUSIONS

We have investigated the processes of secondary initiation for a case observed on 10 July 2004, during the CSIP pilot project. Morcrette *et al.* (2006), which described the observational data from this case, showed that a storm (the ‘primary storm’) generated a cold pool, which initiated an arc of precipitating convection, Arc 1, downwind of the primary storm. Two further arcs of precipitating convection, Arc 2 and Arc 3, formed further downwind, but these were not initiated by cold-pool outflows. A narrower arc (Arc 1a) was also observed to form between Arc 1 and Arc 2. In part I, it was proposed that gravity waves may have been responsible for these other arcs. Using idealized modelling experiments we have shown that convectively generated gravity waves may have first suppressed convection and then initiated these arcs downwind of the primary storm.

The modelling results are consistent with the observations in a number of respects:

- (i) secondary initiation occurs preferentially on the downwind side of the cold pool outflow from the primary storm (due to the deeper head to the cold pool on the downwind side),
- (ii) the fastest convectively generated gravity waves (the  $n = 1$  and  $n = 2$  modes) inhibit convection downwind of the storm until
- (iii) the slower  $n = 3$  mode lowers CIN and initiates arcs of convective cloud downwind of the primary storm.

Furthermore, the modelling results suggest that the dual-peaked nature of the  $n = 3$  mode may be responsible for the two main arcs observed (Arc 2 and Arc 3), although these could also have been caused by multiple cells within the primary storm. The narrower more complex peaks of the  $n = 4$  mode and the cold pool could also have been responsible for the observed Arc 1a. Running the LEM with cloud water but no rain shows that the waves that lower the CIN are generated by the storm, rather than the cold-pool outflow. Without an array of high-precision pressure sensors (resolving surface pressure variations  $\simeq 0.01$  hPa), it is impossible to measure the velocities of any waves that did occur in reality. However, the modelling studies strongly suggest that gravity waves generated by the 'primary storm' significantly affected the timing, depth and spacing of the arcs of convection observed in part I. It appears that the wave effects were especially clear in this case since the lifting of the boundary layer by the waves was sufficient to raise air to its level of free convection, at a time when the other forcing mechanisms present were insufficient to achieve this (e.g. the topographic effects).

The LEM results show that the convectively generated gravity waves had much larger effects at low levels on the downwind side of the primary storm. This appears to have been partly due to the moving wave source (Parker and Burton 2002) and partly from horizontal trapping of the waves. For waves travelling downwind, the Scorer parameter decreased with height, since the Brunt–Väisälä frequency decreased with height and there was an opposing flow above 6 km. This may have led to wave trapping. For waves travelling upwind, wave amplitudes were low below 2 km, since the Scorer parameter was negative below this level.

The modelled effects of gravity waves on the CIN varied continuously with the wind speed applied. Varying the resolution of the LEM showed that, if a high-resolution (1 km or 4 km) non-hydrostatic NWP model forecast the primary storm correctly, it could forecast wave-induced variations in CIN of approximately the correct magnitudes. However, neither the 1 km or the 4 km resolution runs captured the fine-scale variations in CIN well. This suggests that, if the primary storm was forecast or analysed correctly, then an NWP model could capture the approximate location and timing of secondary initiation, if not the details of the convection initiated. In addition, even if a major storm is not well captured by an NWP model, moderate low-level winds and wave trapping should suggest to forecasters that secondary initiation downwind of large storms is possible.

#### ACKNOWLEDGEMENTS

We would like to thank all those involved in the CSIP pilot project: Alan Blyth, Lindsay Bennett, Karl Beswick, Keith Browning, Karen Bozier, Barbara Brooks, Peter Clark, Chris Collier, Fay Davies, Wendy Garland, Martin Gallagher, Charles Kilburn, Darcy Ladd, Cyril Morcrette, Emily Norton, Ed Pavelin, Nigel Roberts, Geraint Vaughan, Ann Webb and Charles Wrench. In particular we would like to thank Keith Browning and Cyril Morcrette for interesting and useful discussions and Cyril Morcrette for providing the Hovmüller diagrams of the Meteosat-8 data. Thanks are also due to the Met Office for providing UM profiles and the radiosonde data. This project was funded by the Natural Environment Research Council (NERC: NER/O/S/2002/00971).

#### REFERENCES

- Bretherton, C. S. and Smolarkiewicz, P. K. 1989 Gravity waves, compensating subsidence and detrainment around cumulus clouds. *J. Atmos. Sci.*, **46**, 740–759

- Crook, N. A. 1988a The effect of ambient stratification and moisture on the motion of atmospheric undular bores. *J. Atmos. Sci.*, **43**, 171–181
- 1988b Trapping of low-level internal gravity waves. *J. Atmos. Sci.*, **45**, 1533–1541
- Einaudi, F., Lalas, D. P. and Perona, G. E. 1978 The role of gravity waves in tropospheric processes. *Pure Appl. Geophys.*, **117**, 627–663
- Erickson, C. O. and Whitney, L. F. 1973 Picture of the month. Gravity waves following severe thunderstorms. *Mon. Weather Rev.*, **101**, 708–711
- Goldstein, S. 1931 On the stability of superposed streams of fluid of different densities. *Proc. R. Soc. London.*, **132A**, 524–548
- Gray, M. E. B., Petch, J., Derbyshire, S. H., Brown, A. R., Lock, A. P. and Swann, H. A. 2001 ‘Version 2.3 of the Met. Office large-eddy model’. Turbulence and Diffusion Notes 275–277, Met. Office, Exeter, UK
- Johnson, R. H., Miner, B. D. and Ciesielki, P. E. 1995 Circulations between mesoscale convective systems along a cold front. *Mon. Weather Rev.*, **123**, 585–599
- Lac, C., Lafore, J. P. and Redelsperger, J. L. 2002 Role of gravity waves in triggering deep convection during TOGA COARE. *J. Atmos. Sci.*, **59**, 1293–1316
- Lane, T. P. and Kniviel, J. C. 2005 Some effects of model resolution on simulated gravity waves generated by deep, mesoscale convection. *J. Atmos. Sci.*, **62**, 3408–3419
- Lane, T. P. and Reeder, M. J. 2001 Convectively generated gravity waves and their effect on the cloud environment. *J. Atmos. Sci.*, **58**, 2427–2440
- Lindzen, R. S. and Tung, K. K. 1976 Banded convective activity and ducted gravity waves. *Mon. Weather Rev.*, **104**, 1602–1617
- Liu, C. and Moncrieff, M. W. 2004 Effects of convectively generated gravity waves and rotation on the organisation of convection. *J. Atmos. Sci.*, **61**, 2218–2227
- Mapes, B. E. 1993 Gregarious tropical convection. *J. Atmos. Sci.*, **50**, 2026–2037
- McAnelly, R. L. and Cotton, W. R. 1997 Upscale evolution of MCSs: Doppler radar analysis and analytical investigation. *Mon. Weather Rev.*, **125**, 1083–1110
- Moncrieff, M. W. and Liu, C. H. 1999 Convection initiation by density currents: Role of convergence, shear, and dynamical organization. *Mon. Weather Rev.*, **127**, 2455–2464
- Morcrette, C. J., Browning, K. A., Blyth, A. M., Bozier, K. E., Clark, P. A., Ladd, D., Norton, E. G. and Pavelin, E. 2006 Secondary initiation of multiple bands of cumulonimbus over southern Britain. I: An observational case-study. *Q. J. R. Meteorol. Soc.*, **132**, 1021–1051
- Nicholls, M. E. and Pielke, R. A. 2000 Thermally induced compression waves and gravity waves generated by convective storms. *J. Atmos. Sci.*, **57**, 3251–3271
- Nicholls, M. E., Pielke, R. A. and Cotton, W. R. 1991 Thermally forced gravity waves in an atmosphere at rest. *J. Atmos. Sci.*, **48**, 1869–1884
- Pandya, R. J., Durran, D. and Bretherton, C. 1993 Comments on ‘Thermally forced gravity waves at rest’. *J. Atmos. Sci.*, **50**, 4097–4101
- Parker, D. J. and Burton, R. R. 2002 The two-dimensional response of a tropical jet to propagating lines of convection. *J. Atmos. Sci.*, **59**, 1263–1273
- Scorer, R. S. 1949 Theory of waves in the lee of mountains. *Q. J. R. Meteorol. Soc.*, **75**, 41–56
- Shige, S. and Satomura, T. 2001 Westward generation of eastward-moving tropical convective bands in TOGA COARE. *J. Atmos. Sci.*, **58**, 3724–3740
- Taylor, G. I. 1931 Effect of variation of density on the stability of superposed streams of fluid. *Proc. R. Soc. London*, **132A**, 499–523
- Wang, T. and Li, Y. 1999 Wave ducting in a stratified shear flow over a two-dimensional mountain. Part I: General linear criteria. *J. Atmos. Sci.*, **56**, 412–436